PAPER

View Article Online
View Journal | View Issue

High-pressure polymorph of Co₃P₂O₈: phase transition to an olivine-related structure

Robin Turnbull, [a] Josu Sánchez Martín, [a] Akun Liang, [a,b]
Daniel Díaz-Anichtchenko, [a] Catalin Popescu, [c] K. Sandeep Rao, [d]
S. Nagabhusan Achary, [d] Alfonso Muñoz, [e] Vinod Panchal[f] and
Daniel Errandonea *[a]

The monoclinic polymorph of Co₃P₂O₈ (space group P2₁/c), isomorphic to farringtonite (Mg₃P₂O₈) type orthophosphates, was studied up to 21 GPa using synchrotron powder X-ray diffraction and density-functional theory simulations to investigate the influence of pressure in the crystal structure. This study revealed a pressure induced structural phase transition for monoclinic cobalt phosphate, Co₃P₂O₈, and the details of crystal structure of the new high-pressure polymorph were delineated. The evolution of XRD pattern with pressure indicate that the onset of a phase transition occurs around 2.90(5) GPa, and the low- and high- pressure phases coexist up to 10.3(1) GPa. The high-pressure phase also has a monoclinic lattice (space group P2₁/c), and a discontinuous change of unit-cell volume of about 6.5% occurs at the transition. A reorganization of atomic positions with a change in the cobalt coordination sphere occurs in the phase transition. Notably, the high-pressure polymorph has a defect-olivine-type structure like chopinite-type orthophosphates. Using a third-order Birch–Murnaghan equation of state, the bulk moduli of the low pressure (LP) phase (75(2) GPa) and high-pressure (HP) phase (92(2) GPa) were determined. For the low-pressure polymorph, the principal axes of compression and their compressibility were also determined. Density-functional theory calculations also provided the frequencies of Raman- and infrared-active modes which can be used for mode assignment in future experiments.

I. Introduction

The A₃B₂O₈-type orthovanadates and orthophosphates (A = divalent cation) show varieties of structure types depending on the ionic radii of the A cation as well as preparation conditions or external thermodynamic parameters like pressure and temperature.[1–3] Owing to the presence of isolated vanadate or phosphate groups, they often form loosely packed and flexible crystal structure, and hence varieties of functional properties relevant for several technological applications like laser-host, phosphors, scintillators, display devices, ion transportation, and catalysis or photocatalysis, *etc.* can be expected or intro-

duced in such materials.[4–9] For larger divalent cations (A²⁺) like alkaline earth or lead cations, the A₃B₂O₈ type vanadates or phosphates usually form palmierite, apatite and related structures.[2,3,10] Such compositions can have centrosymmetric or non-centrosymmetric lattices. They are known to show high dielectric constant with low loss character, microwave dielectric properties, and ferroelectric properties. For the smaller, A²⁺ ions, they form relatively denser and distorted kagome structures, and hence display severely altered electronic properties and optical properties depending on the nature of A²⁺ ions.[7,8,11–16]

Rich polymorphism under pressure with the existence of newer phases and contrasting sequences of phase transitions depending on the divalent element A has been documented for several of such A₃B₂O₈-type vanadates and phosphates. This fact has been well understood in the compounds of orthovanadate family.[11–18] Among these compounds, Cu₃V₂O₈ decomposes into CuO and V₂O₅ at 1.35 GPa,[13] while Ca₃V₂O₈, Mn₃V₂O₈ and Sr₃V₂O₈, undergo phase transitions at 9.8,[15] 10,[16] and 13.8 GPa,[2] respectively. However, Zn₃V₂O₈, Ni₃V₂O₈, Co₃V₂O₈, and Ba₃V₂O₈ do not exhibit any phase transition up to at least 15,[14] 23,[12] 20,[12] and 29 GPa,[3] respectively. In contrast to their vanadate counterparts, only limited studies on

a Departamento de Física Aplicada-ICMUV, Universidad de Valencia, Dr Moliner 50, Burjassot, 46100 Valencia, Spain. E-mail: daniel.errandonea@uv.es
b Centre for Science at Extreme Conditions and School of Physics and Astronomy, University of Edinburgh, EH9 3FD Edinburgh, UK
c CELLS-ALBA Synchrotron Light Facility, Cerdanyola del Vallès, 08290 Barcelona, Spain
d Chemistry Division, Bhabha Atomic Research Centre (BARC), Trombay, Mumbai 400 085, India
e Departamento de Física, MALTA-Consolider Team, Universidad de La Laguna, San Cristóbal de La Laguna, E-38200 Tenerife, Spain
f Department of Physics, Royal College, Mumbai 401107, India

the HP behaviour of the analogous phosphates are reported in literature.[19–23] Information on the high-pressure behaviour of such phosphates and the structure of high-pressure phases are mainly available on the minerals, like, sarcopside, $(Fe,Mn,Mg)_3(PO_4)_2$, chopinite, $[(Mg,Fe)_3](PO_4)_2$, and related orthophosphates.[19–25] It has been suggested that these denser polymorphs have a defective olivine-type structure and are formed by combined effects of temperature and pressure on farringotoinite by a meteoritic strike.[23–26] Thus, they also can be probably synthesized by HP-HT techniques as metastable phases.[23,26,27] Most of these studies were focused on Mg^{2+} or Fe^{2+} containing orthophosphates due to their mineralogical relevance. However, to the best of our knowledge analogous orthophosphates with smaller transition metal ions are not explored under pressure. It is well known that pressure not only affects the structural properties but also modifies bond distances and angles in the structure. Thus, it can be used to tune the vibrational and electronic properties conveniently.[28] In some cases, application of pressure can lead to the discovery of new metastable phases with interesting physical properties that can be achieved at ambient conditions, and hence can open new opportunities for applications.[1,29] To understand the effect of pressure on a transition metal ion bearing phosphates, a systematic study on cobalt orthophosphate, $Co_3P_2O_8$, under high-pressure conditions up to 20 GPa at room temperature was undertaken.

$Co_3P_2O_8$ crystallizes in a monoclinic structure described by space group $P2_1/c$ (it is also described in the literature by the non-standard space group $P2_1/n$).[30] It is isostructural with γ-$Zn_3(PO_4)_2$[31] and $Mg_3(PO_4)_2$,[32] farringtonite-type orthophosphates.[30] The crystal structure of ambient pressure phase of $Co_3P_2O_8$ is depicted in Fig. 1a. In the structure, cobalt atoms occupy two different coordination polyhedra, a slightly distorted octahedron (CoO_6) and a penta-coordinated polyhedron (CoO_5), in a ratio of one to two respectively. The penta-coordinated CoO_5 polyhedron can be described as a distorted trigonal bipyramid. The presence of such polyhedra in related vanadates, like $Zn_3V_2O_8$, has been related to the existence of pressure induced phase transitions.[14] $Zn_3V_2O_8$ undergoes a

phase transition by hydrostatic pressure below 4 GPa, which has been attributed to the displacement of an oxygen atom towards ZnO_5 units under the influence of pressure and that leads to a closely packed structure and transforms the ZnO_5 units to ZnO_6 octahedral units. We hypothesized that such structural changes could be a common phenomenon in such orthovanadates and phosphates, and that further motivate us to explore the high-pressure behaviour and possible pressure induced phase transitions in $Co_3P_2O_8$, which has not yet been studied under compression. In fact, $Co_3P_2O_8$ is also scarcely studied at ambient conditions and more commonly investigated in the interest of its use as a pigment in ceramics, (it was the favourite violet pigment of Claude Monet who used it in the famous Water-Lilies painting[33]), as a catalytic material,[34] as an electrode in super-capacitors when hydrated,[35] as well as due to its interesting magnetic properties.[36,37] However, neither experimental nor theoretical data on its mechanical properties or lattice vibrations are reported in literature.

To understand the properties and HP behaviour of $Co_3P_2O_8$, we have performed a combined *in situ* HP powered X-ray diffraction (XRD) measurements as well as density-functional theory (DFT) calculations. A structural phase transition was discovered at 2.90(5) GPa, and the crystal structure of the new phase has been determined. Compressibility, elastic constants and bulk moduli for both ambient and high-pressure phases were obtained experimentally and theoretically. The frequencies and assignments of Raman- and infrared-active modes for both ambient and high-pressure phases have been calculated, and to our believes these are being reported for the first time.

II. Materials and methods

$Co_3P_2O_8$ was prepared by a multistep reaction of Co_3O_4 (Alfa Aesar, 99.9%) and $(NH_4)_2HPO_4$ (Thomas Baker, 99.5%). All the reactants were used as received. The weighed quantities of the reactants were thoroughly mixed and heated at 300 °C on a
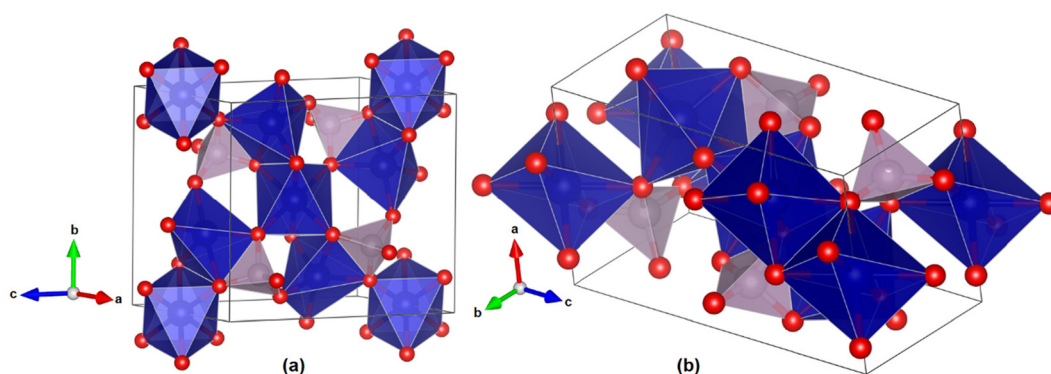
Fig. 1 The crystal structure of (a) the ambient-pressure phase of $Co_3P_2O_8$, and (b) the high-pressure phase of $Co_3P_2O_8$. The CoO_5 and CoO_6 polyhedra are shown in blue and the VO_4 tetrahedra are shown in grey. The red circles represent the oxygen atoms. The unit-cell is represented with black solid lines.

hotplate using a platinum crucible. The mixture was heated until the complete melting and decomposition of $(NH_4)_2HPO_4$ was ensured. Once cooled, the solidified mass was then homogenized, pressed into pellet and then heated at 750 °C for 12 h. This step was repeated after homogenization of the product. Further the sample was crushed and pressed to pellet and heated at 900 °C for 5 h. All the heat treatments were carried out in air using a platinum boat as sample holder. A crystalline single phase monoclinic $Co_3P_2O_8$ was confirmed from powder XRD measurements of the sample. The ambient pressure unit-cell parameters observed from the powder XRD data are: a_0 = 5.0629(5) Å, b_0 = 8.3611(8) Å, c_0 = 8.7882(8) Å, and β_0 = 121.0(5)°, and they agree with crystal structure reported in literature.[24,30]

High-pressure angle-dispersive powder XRD experiments were performed at ambient temperature at the Materials Science and Powder Diffraction beamline (BL04-MSPD) of ALBA synchrotron.[38] We employed a membrane-type diamond-anvil cell (DAC) with diamond culets of 500 μm in diameter. A 200 μm thick Inconel gasket, pre-indented to a thickness of 50 μm, with a 250-μm diameter hole drilled in the center was used as the pressure chamber. A mixture of methanol–ethanol–water (16 : 3 : 1) was used as the pressure-transmitting medium (PTM). This PTM remains quasi-hydrostatic up to 10 GPa,[39] but it has been successfully used to study high pressure behavior of oxides up to significantly higher pressure than that of the present study.[40] A Cu grain was loaded next to the sample in DAC to use as pressure marker. Pressure at the sample was determined from the position of the Cu 111 reflection in the XRD pattern and the equation of state (EOS) for Cu reported by Dewaele et al.[41] During the process of sample loading, great attention was given to ensure that only a minor portion of the pressure chamber was occupied by the loaded sample and Cu. This was done to minimize the likelihood bridging between sample and diamond anvils. For HP XRD, a monochromatic X-ray beam of wavelength 0.4642 Å focused down to a spot size of 20 × 20 μm (full-width-at-half-maximum) and collimated with a pinhole. XRD images were collected on a two-dimensional Rayonix SX165 CCD detector. The two-dimensional diffraction images were integrated using DIOPTAS.[42] Rietveld refinements were performed using FullProf software package.[43]

Total-energy *ab initio* simulations were performed within the framework of density-functional theory, DFT,[44] with the Vienna *ab initio* Simulation Package, VASP.[45,46] In this study we utilized projector augmented-wave (PAW) pseudopotentials[47,48] and extended the plane-wave kinetic cut-off up to 540 eV to guarantee highly converged outcomes. The integrations over the Brillouin zone, BZ, were carried out with k-special points samplings (6 × 4 × 4 and 4 × 6 × 6 grids for the low- and high-pressure phases, respectively). The exchange–correlation energy was described by means of the generalized-gradient approximation, GGA, with the Armiento and Mattsson, AM05, prescription.[49] To treat the strongly correlated states appropriately, the DFT+U method of Dudarev et al.[50] was employed. This method utilizes a single parameter, $U_{eff} = U - J$, where U

and J are the effective on-site Coulomb and exchange parameters, respectively. The value of U_{eff} for the Co atoms used was 3.32 eV.[51] In the present study, the antiferromagnetic configuration was found to be the lower energy one. The unit-cell parameters and the atomic positions were fully optimized to obtain the relaxed structure at selected volumes. The criteria imposed for the optimization process were that the forces on the atoms should be smaller than 0.003 eV Å^{-1} and the deviations of the stress tensors from a diagonal hydrostatic form were smaller than 0.1 GPa. In this manner, the simulations provide a data set of volumes, energies, and pressures (from the stress tensor). These were fitted with a third-order Birch–Murnaghan equation of state[52] to obtain theoretical equilibrium volume, bulk modulus and its pressure derivative. Lattice-dynamic calculations of the phonon modes were carried out at the zone centre (Γ point) of the BZ with the direct force-constant approach.[53] These calculations give the frequencies of the normal modes, their symmetries, and their polarization vectors. This allows the identification of the irreducible representations and the character of the phonon modes at the Γ-point. A 2 × 2 × 2 supercell was used to obtain the phonon dispersion and to check the dynamical stability of the analysed structures. Mechanical properties were studied from the calculations of the elastic constants using the stress–strain methodology implemented in VASP using the Le Page[54] methodology. From these elastic constants, we derived the different elastic moduli and analyzed the mechanical stability.

III. Results and discussion

A. XRD experiments

We performed two HP XRD experiments, one up to 20.60(5) GPa (experiment 1) and the another (experiment 2) only up to 4.60(5) GPa. In the first experiment we observed the onset of a phase transition at 2.90(5) GPa. The second experiment was performed only up to pressures slightly above the transition pressure to confirm the results of the first experiment and to collect more data for the EOS determination of the low-pressure phase. In experiment 2, the transition pressure was 2.85(5) GPa, which agrees with the first experiment. In Fig. 2, we present a selection of HP XRD patterns recorded in the first experiment at different pressure conditions. In the figure, it can be seen that XRD patterns at 0.30(5) and 2.20(5) GPa agree well with a crystal structure (low-pressure, LP) isomorphic to that of the farringtonite-type phase. Rietveld refinement plots are included to support this statement. The goodness of fit parameters for the experiment performed at 0.30(5) GPa are R_p = 2.85%, R_{wp} = 3.62%, and χ^2 = 1.24. Similar values were obtained for the low-pressure phase in both experiments at different pressures confirming the correctness of the structural model. The refined crystal structure parameters at 0.15(5) GPa are given in Table 1, and the corresponding CIF file can be downloaded from the Cambridge Crystallographic Data Centre (CCDC), using the deposition number 2354014. The present observed crystal structure is very similar to the structure of
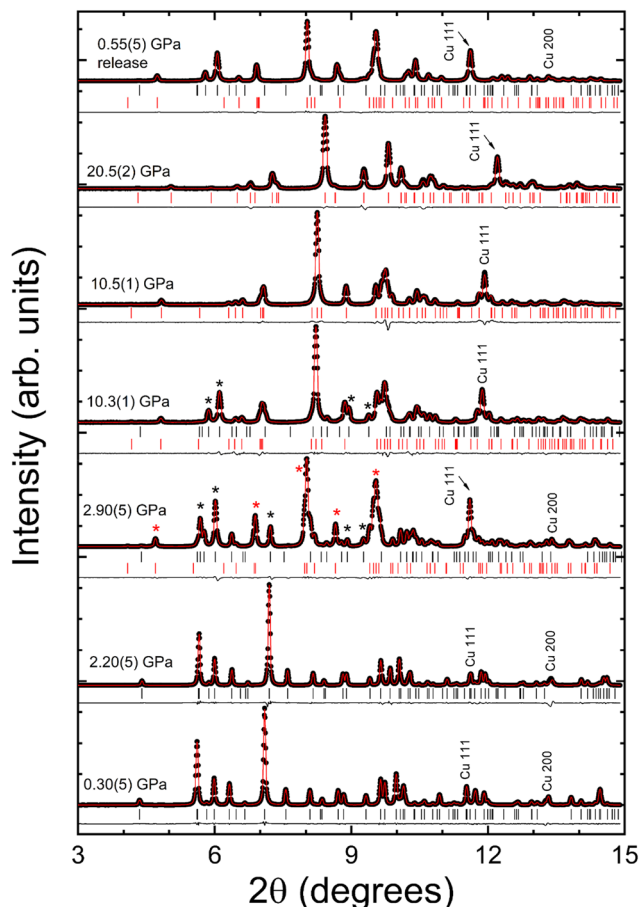
Fig. 2 Rietveld refinement profiles of powder XRD patterns measured in $Co_3P_2O_8$ at selected pressures shown in the figure. Pressures are given in the figure with the uncertainties given between brackets. The black circles are the experimental data, and the red (black) lines are the refinements (residuals). Vertical black (red) ticks are the calculated positions of the reflections of the low(high)-pressure phase. The Cu peaks used to measure pressure are indicated. Black (red) asterisks are the peaks of the low(high)-pressure phase discussed in the text.

Table 1 Experimental unit-cell parameters, atomic positions, and bond-distances (in Å) of the low-pressure phase of $Co_3P_2O_8$ at 0.15(5) GPa. CCDC 2354014

$a = 5.0635(1)$ Å, $b = 8.3594(2)$ Å, $c = 8.7865(2)$ Å, and $\beta = 121.05(2)°$

Atom	Site	x	y	z
Co1	4e	0.5169(4)	0.8589(4)	0.6119(10)
Co2	2b	0.5	0	0
P	4e	0.8385(2)	0.1940(2)	0.8006(2)
O1	4e	0.7687(9)	0.1424(9)	−0.0549(9)
O2	4e	0.1882(9)	0.1956(4)	0.8739(4)
O3	4e	0.6875(4)	0.3637(4)	0.7419(4)
O4	4e	0.6888(4)	0.0775 (5)	0.6410(4)

P–O2 = 1.542(5), P–O1 = 1.545(9), P–O4 = 1.547(4), and P–O3 = 1.567(4). Co1–O2 = 1.976(6), Co1–O4 = 1.979(9), Co1–O4 = 1.983(5), Co1–O3 = 2.023(9), and Co1–O1 = 2.207(6). Co2–O2 = 2.143(4) ($x2$), Co2–O1 = 2.044(8) ($x2$), and Co2–O3 = 2.153(4) ($x2$).

$Co_3P_2O_8$ reported at ambient conditions[24,30] with only small changes in lattice parameters and atomic positions. Relevant bond distances in the structure are given in Table 1. They agree with those previously reported in the literature[24,30] at ambient conditions.

In experiments 1 and 2, we detected the appearance of extra diffraction peaks at 2.90(5) GPa and 2.85(5) GPa, respectively. This can be seen in Fig. 2 which depicts the data from experiment 1. Some of the more prominent additional peaks are marked with red asterisks in Fig. 2. In the same figure at 2.90(5) GPa we identify with black asterisks peaks that undoubtedly belong to the low-pressure phase. We associated the appearance of extra peaks as the onset of a structural phase transition. As pressure was increased, we found that the peaks of the low-pressure phase became weaker, and the peaks of the high-pressure phase became stronger. However, there are peaks of the low-pressure phase that can be identified up to 10.3(1) GPa. They are denoted by black asterisk in Fig. 2. The peaks of the low-pressure phase completely disappear at 10.5(1) GPa supporting the completion of the phase transition. We believe the coexistence of the low-pressure and high-pressure phase might be connected to a kinetic barrier similar to that observed in the related phosphate, $LiNiPO_4$.[55] As we will describe below, the reported phase transition is reconstructive involving the modification of primary chemical bonds. Consequently, the phase transformation needs to overcome an energy barrier (the kinetic barrier) which makes the transition slow and favours the coexistence of the low- and high-pressure phases. The phase coexistence is not due to non-hydrostatic conditions or pressure gradients because in this pressure range the conditions are quasi-hydrostatic.[39] This argument is consistent with the fact that there is no significant peak broadening in the XRD experiment under HP.

For the structural assignation of the HP phase, we first indexed the XRD pattern measured at 10.5(1) GPa using DICVOL[56] and then assigned the symmetry. It is found that the space group $P2_1/c$ gives the best figure of merit, and that the unit-cell parameters determined after indexation resembled those of the metastable olivine-type $Co_3P_2O_8$ reported by Berthet *et al.* which is isostructural to chopinite.[27] Then, we refined the atomic positions by Rietveld refinement method using atomic positions reported by Berthet *et al.*[27] as initial position coordinates. Fig. 2 shows the Rietveld refinement plot for the XRD data obtained at 10.5(1) GPa. The refined structure gives small residuals and goodness-of-fit parameters, $R_p = 2.85\%$, $R_{wp} = 4.44\%$, and $\chi^2 = 1.57$. The unit-cell parameters and atomic position determined at 10.5(1) GPa are summarized in Table 2. This table also include bond distances which are similar to those reported at ambient pressure in the literature.[27] The CIF file can be downloaded from CCDC under deposition number 2355641. The crystal structure of the HP phase is shown in Fig. 1b. In the structure of HP phase, all the Co atoms are in octahedral coordination. The relevant bond distances are given in Table 2. XRD patterns measured upon further compression can be fitted with the same structural model as shown in Fig. 2 for the measurement at 20.5(2)

Table 2 Experimental unit-cell parameters, atomic positions, and bond-distances (in Å) of the HP phase of $Co_3P_2O_8$ at 10.50(5) GPa. CCDC 2355641

$a = 5.7858(1)$ Å, $b = 4.7475(2)$ Å, $c = 9.9344(2)$ Å, and $\beta = 91.72(2)°$				
Atom	Site	x	y	z
Co1	2b	0.5	0	0
Co2	4e	0.7616(9)	0.5143(9)	0.2279(9)
P	4e	0.7471(9)	0.0753(9)	0.4058(9)
O1	4e	0.7316(15)	0.7481(15)	0.4013(15)
O2	4e	0.7493(15)	0.3057(15)	0.0487(15)
O3	4e	−0.0544(15)	0.1932(15)	0.3233(15)
O4	4e	0.5296(15)	0.2281(15)	0.3377(15)

P–O2 = 1.528(17), P–O3 = 1.536(13), P–O1 = 1.557(9), and P–O4 = 1.586 (12). Co1–O1 = 2.055(11) (x2), Co1–O4 = 2.077(13) (x2), and Co1–O2 = 2.093(9) (x2). Co2–O3 = 1.975(11), Co2–O2 = 2.037(16), Co2–O4 = 2.056 (11), Co2–O1 = 2.061(16), Co2–O3 = 2.072(12), and Co2–O4 = 2.219(13).

GPa. After decompression, at the lowest pressure, the recovered sample contained both the HP and LP phases, supporting the hypothesis that the transition might be hindered by a kinetic barrier.[57]

The observed phase transition involves a structural reorganization and an abrupt decrease of the unit-cell volume, as discussed below. These observations suggest the phase transformation is a first-order reconstructive phase transition. An important structural change in the phase transformation is related to the coordination number of Co atoms. The low-pressure phase the $Co1O_6$ octahedra and $Co2O_5$ units share edges to form a zig-zag –$Co1O_5$–$Co2O_6$–$Co1O_5$– chain. In contrast, the high-pressure phase has a closely similar framework formed by edge sharing $Co2O_6$–$Co1O_6$–$Co2O_6$ octahedral chains. The presence of penta-coordinated Co ions near a vacant coordination site is conducive to the formation of additional Co–O bonds at relatively low compression, thereby favouring the observed phase transition. The high-pressure phase is an olivine-type structure with ordered vacancies. The structure can be seen as a monoclinic distortion of orthorhombic $Co_2Li_2P_2O_8$ (space group *Pnma*),[58] where the two Li atoms are substituted by one cobalt atom and a vacancy, forming $[Co_3\square]$ P_2O_8. The presence of ordered vacancies favors tilting of CoO_6 octahedra which triggers the reduction of symmetry of the crystal structure. In fact, the HP chopinite-type structure can be obtained by a group–subgroup transformation from the structure of $Co_2Li_2P_2O_8$ by letting the β angle deviate from 90°. The occurrence of the observed phase transition is consistent with the fact that chopinite has been found as a HP polymorph of Mg-dominant farringtonite in meteoritic minerals found in Antarctica.[23]

From the Rietveld refinements of the XRD patterns acquired on sample compression, we determined the pressure dependence of the unit-cell parameters. The pressure dependence of the unit-cell parameters is presented in Fig. 3. In the figure, we also show the results from density functional theory (DFT) calculations for comparison. DFT calculated results agree quite well with experiments for the LP phase. For the HP
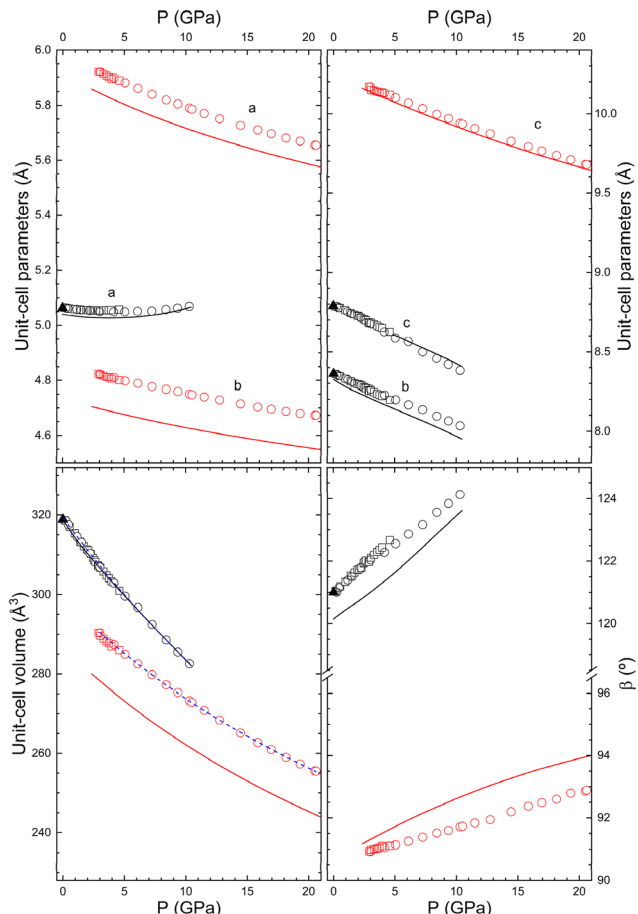

Fig. 3 Pressure dependence of the unit-cell parameters a, b, c, and β and volume, for both the LP and HP phases of $Co_3P_2O_8$. Empty circles (squares) are from experiment 1 (2). The black triangles are the results at ambient conditions. Black (red) colour is used for the LP (HP) phase. The solid lines are the results from DFT simulations, and the dashed blue lines are the equations of state fitted to the experimental data described in the text. The associated errors are smaller than symbols.

phase the calculated data show slightly underestimated lattice parameters a, b, and c while a slightly overestimated angle β. As a consequence, the volume is underestimated by 3% in DFT simulations. This difference is typical of DFT calculations performed within the GGA approximation as it is related to the approximation used to describe the exchange–correlation energy. Such differences are also observed in the elastic constants. The causes for such differences have historically been discussed in the literature.[59,60] In the LP phase the parameter a follows a non-linear behaviour, decreasing up to around 3 GPa (*i.e.*, the transition pressure) and then increasing with pressure. The other two parameters have a similar compressibility, and the angle β increases with pressure enhancing the monoclinic distortion of the structure. In the HP phase, a, b, and c have a similar compressibility and β increases with pressure. Regarding the pressure dependence of the volume, in both phases we found that it can be described by a third-order Birch–Murnaghan equation of state (BM EOS).[52]

According to the fits shown in Fig. 3, for the LP phase the experimental unit-cell volume at zero pressure, bulk modulus, and its pressure derivative are: $V_0 = 319.3(2)$ Å^3, $B_0 = 75(2)$ GPa, and $B'_0 = 2.1(3)$, respectively, while the corresponding values for the HP phase are: $V_0 = 299.4(2)$ Å, $B_0 = 92(2)$ GPa and $B'_0 = 4.2(2)$. The increase in B_0 and B_0' after the phase transition

indicates a decrease of the compressibility, which is consistent with the abrupt decrease of the volume by 6.5%, which makes the HP phase denser than the LP phase. The discontinuity of the volume at the phase transition is consistent with a first-
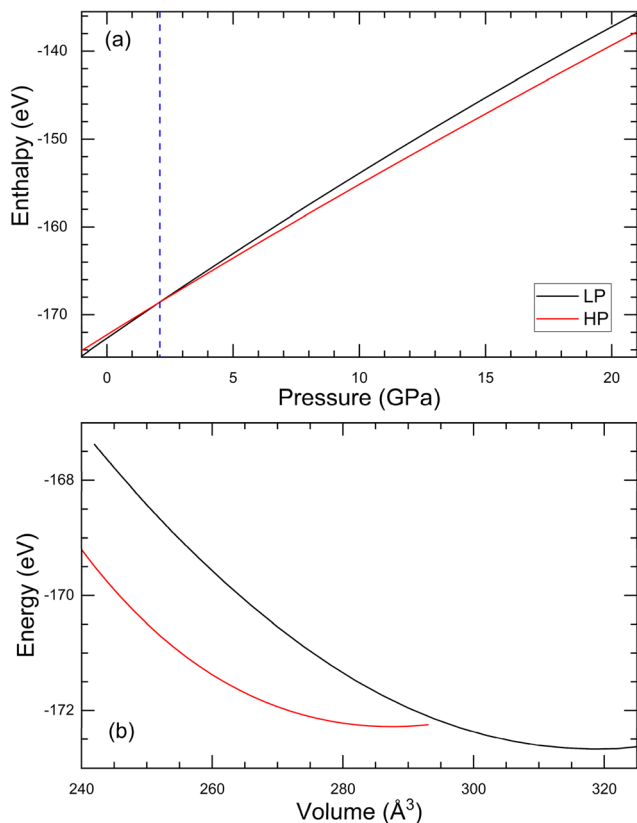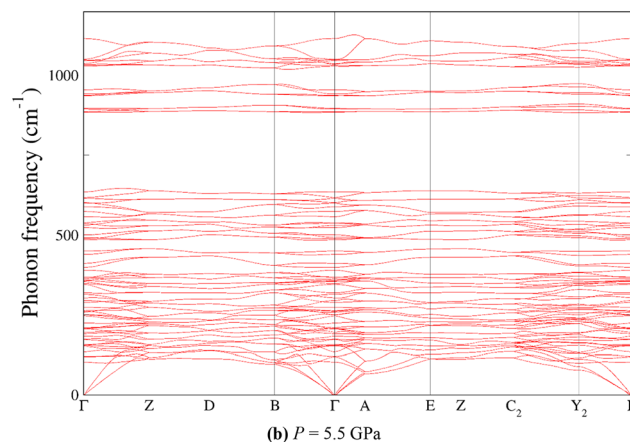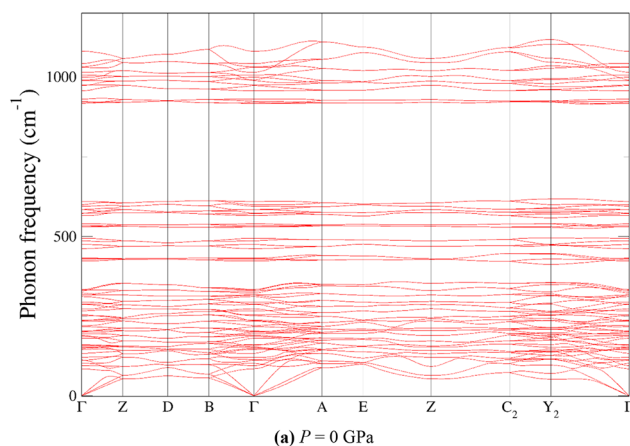

Fig. 4 (a) DFT calculated enthalpy *vs.* pressure for the low-pressure (black) and high-pressure (red) phases of $Co_3P_2O_8$. The vertical blue dashed line shows the pressure where the enthalpy curves cross intersect. (b) DFT calculated energy *vs.* volume for the same phases. To identify phases in (b), we have used the same colour code than in (a).

Table 4 Calculated elastic constants C_{ij} (in GPa) for HP $Co_3P_2O_8$ at 0 GPa. The bulk (B), shear (G), and Young (E) moduli, Poisson's ratio (*n*), and B/G ratio are also included. B, G, and E are given in GPa

C_{ij}		Property	
C_{11}	133.5	B	100.7
C_{22}	202.5	G	48.8
C_{33}	206.1	E	126.1
C_{44}	59.1	ν	0.291
C_{55}	37.8	B/G	2.06
C_{66}	44.9		
C_{12}	57.1		
C_{13}	66.1		
C_{15}	−8.2		
C_{23}	80.4		
C_{25}	−17.7		
C_{35}	−11.2		
C_{46}	−13.6		

Table 3 Calculated elastic constants C_{ij} (in GPa) for LP $Co_3P_2O_8$ at 0 GPa. The bulk (B), shear (G), and Young (E) moduli, Poisson's ratio (*n*), and B/G ratio are also included. B, G, and E are given in GPa

C_{ij}		Property	
C_{11}	184.5	B	80.6
C_{22}	129.3	G	34.4
C_{33}	100.6	E	90.4
C_{44}	39.0	ν	0.313
C_{55}	30.1	B/G	2.34
C_{66}	32.9		
C_{12}	77.4		
C_{13}	66.7		
C_{15}	−2.8		
C_{23}	40.1		
C_{25}	3.4		
C_{35}	−13.8		
C_{46}	−0.7		

Fig. 5 Phonon dispersion of (a) the low-pressure phase of $Co_3P_2O_8$ at 0 GPa and (b) the high-pressure phase of $Co_3P_2O_8$ at 5.5 GPa.

order nature for the transition and consistent with coexistence of both LP and HP phases in wider pressure range. The bulk modulus we report for LP $Co_3P_2O_8$ (farringtonite-type) is similar to that of α-$Ca_3P_2O_8$ (B_0 = 79(2) GPa and B'_0 = 4).[61] The bulk modulus of HP $Co_3P_2O_8$ (chopinite-type) is similar to that reported recently for isostructural $Mg_3P_2O_8$ (B_0 = 82(2) GPa and B'_0 = 4),[62] $Sr_3P_2O_8$ (B_0 = 89(2) GPa and B'_0 = 6.6(3)),[63] and olivine-type $LiNiPO_4$ (B_0 = 88(2) GPa and B'_0 = 3.5(5)).[55] Among related phosphates, only compounds where one of the cations is potassium are more compressible, such as $K_2Ce(PO_4)_2$ (B_0 = 52(3) GPa and B'_0 = 5.7(6)).[64] This is because of the relative weakness of K–O bonds which exhibit significant compressibility under pressure.

B. DFT calculations

In Fig. 4 we present the enthalpy *versus* pressure, and energy *versus* volume (inset) for the LP and HP phases of $Co_3P_2O_8$.

The calculations show that LP farringtonite-type $Co_3P_2O_8$ is the structure with the lowest energy and lowest enthalpy at 0 GPa. Thus, the farringtonite-type structure is the thermodynamically most favourable structure of $Co_3P_2O_8$. As pressure increases, the volume decreases, and beyond 2.1 GPa, the HP chopinite-type structure becomes the most stable structure for $Co_3P_2O_8$. These results support the occurrence of a structural phase transition at 2.1 GPa in agreement with experiments. From calculations we determined the EOS parameters for both phases as: V_0 = 318.4(2) $Å^3$, B_0 = 78(2) GPa, and B'_0 = 2.0(3) (for low-pressure phase) and V_0 = 286.9(2) $Å^3$, B_0 = 91(1) GPa, and B'_0 = 4.2(2) (for high-pressure phase). The values of the bulk moduli and their pressure derivatives are also consistent with those extracted from experiments.

Our calculations also support the mechanical and dynamical stability of the two structures. Tables 3 and 4 show the calculated elastic constants for both structures. All the eigen-

Table 5 Calculated optical phonon frequencies ω (in cm^{-1}) at the Γ point for the low-pressure phase of $Co_3P_2O_8$ at 0 GPa and the high-pressure phase at 5.5 GPa

Low pressure phase				High pressure phase			
Raman		IR		Raman		IR	
Mode	ω	Mode	ω	Mode	ω	Mode	ω
B_g	95.4	A_u	83.6	B_g	111.2	A_u	90.9
A_g	102.8	B_u	111.7	A_g	113.5	B_u	126.9
A_g	114.2	A_u	120.0	B_g	143.5	B_u	149.1
A_g	145.1	B_u	132.7	A_g	146.4	A_u	150.6
B_g	152.0	A_u	148.9	A_g	159.9	A_u	168.6
A_g	157.6	B_u	153.9	B_g	181.1	B_u	188.8
B_g	160.4	A_u	180.1	B_g	193.9	A_u	191.9
A_g	201.4	A_u	186.4	A_g	200.9	A_u	203.6
B_g	202.2	B_u	188.8	A_g	235.5	B_u	206.1
B_g	216.5	B_u	194.5	B_g	244.4	A_u	213.6
A_g	234.9	A_u	200.0	A_g	254.1	B_u	240.4
B_g	235.9	A_u	219.7	B_g	265.9	B_u	253.3
A_g	267.1	B_u	234.2	A_g	291.8	A_u	253.7
A_g	287.8	A_u	250.7	A_g	309.5	A_u	285.0
B_g	294.9	B_u	254.2	B_g	311.9	B_u	292.1
B_g	312.5	A_u	272.3	B_g	333.6	A_u	343.5
B_g	321.9	B_u	286.7	A_g	334.2	B_u	344.9
A_g	332.7	A_u	316.9	B_g	349.9	A_u	353.4
B_g	421.8	B_u	316.9	A_g	388.9	A_u	356.0
A_g	431.4	B_u	329.3	B_g	397.8	B_u	358.0
A_g	461.5	A_u	332.6	A_g	477.3	B_u	380.5
B_g	474.7	B_u	427.7	B_g	491.0	A_u	433.7
B_g	528.6	A_u	430.7	A_g	525.8	B_u	442.4
A_g	532.4	A_u	485.9	B_g	534.2	A_u	485.8
A_g	572.1	B_u	493.7	A_g	583.7	B_u	489.2
B_g	584.0	B_u	529.0	B_g	595.2	A_u	517.6
A_g	584.3	A_u	538.9	A_g	612.2	B_u	532.2
B_g	594.6	A_u	564.8	B_g	626.2	B_u	553.7
A_g	919.6	B_u	572.4	B_g	885.1	A_u	565.8
B_g	928.8	B_u	598.9	A_g	893.2	A_u	595.4
A_g	972.6	A_u	609.1	B_g	934.2	B_u	609.2
A_g	989.7	A_u	916.1	A_g	940.4	B_u	881.6
B_g	1004.5	B_u	922.3	B_g	1025.5	A_u	891.4
A_g	1032.1	A_u	955.4	A_g	1027.2	B_u	933.7
B_g	1041.3	B_u	973.4	A_g	1041.2	A_u	952.4
B_g	1079.9	B_u	988.1	B_g	1048.0	B_u	1031.0
		A_u	998.2			A_u	1033.9
		B_u	1014.3			B_u	1050.3
		A_u	1029.4			A_u	1114.1

values of both elastic tensors are positive indicating elastic stability of both phases. The obtained constants also fulfil the Born criteria[65] and confirm that the structures are mechanically stable. From the elastic constants, we have calculated the elastic moduli using the average between the values obtained with the Hill and Reuss approximations.[66] The obtained bulk moduli for the low-pressure (80.6 GPa) and high-pressure phases (100.7 GPa) agree with the values obtained from experiments and total-energy calculations. The Young's modulus, in the low(high)-pressure phase is 12% (20%) larger than the bulk modulus, indicating that in both phases the tensile and compressive stiffness when the force is applied lengthwise is larger than their resistance to bulk compression. We also found that in both phases the shear modulus is considerably smaller than the bulk modulus indicating that shear deformations are favoured over volume contraction, making both phases of $Co_3P_2O_8$ susceptible to large non-hydrostatic stresses.[67] In addition, according to the B/G ratio (>1.75), we can postulate that the two phases of $Co_3P_2O_8$ are ductile.[68] The values of the Poisson's ratio (ν) are also consistent with this conclusion.[69]

To conclude, we present the results of our phonon calculations. The calculated phonon dispersion of each phase is shown in Fig. 5. The phonon dispersions indicate that there are no imaginary phonon branches in the structures examined in this study. This provides evidence for the dynamic stability of the two phases of $Co_3P_2O_8$. We have also calculated the phonon frequencies and the symmetries for the Raman-active and infrared (IR)-active modes. The results are summarized in Table 5. Since there are no Raman or IR experiments reported for the studied materials, our results can be used as a guide for future experiments. Using group theory, the following 78 vibrational modes are predicted for both phases at the Γ point of the BZ; $\Gamma = 18A_g + 18B_g + 21A_u + 21B_u$. Of these modes, one A_u mode and two B_u modes are the acoustic modes. All of the remaining modes are optical modes. Out of the modes present, 36 can be observed in Raman spectroscopy ($18A_g + 18B_g$), and 39 can be observed in IR spectroscopy ($20A_u + 19B_u$). In the low-pressure phase, the distribution of Raman modes resembles the Raman spectra of $Mg_3P_2O_8$[69] and $Ca_3P_2O_8$.[70] A principal characteristic of the Raman and IR spectra of the low-pressure phase is the phonon gap from 600 to 915 cm^{-1}. This is related to the fact that modes above 915 cm^{-1} are associated to internal vibrations of the PO_4 tetrahedron. The rest of the modes correspond mainly to lattice vibrations involving Co atoms and PO_4 tetrahedra moving as rigid units. Among the internal modes the A_g modes with frequencies of 987.7 and 1032.1 cm^{-1} are the symmetric and asymmetric stretching modes of the PO_4 tetrahedron. Note that their frequencies are nearly the same as those observed for the equivalent modes in $Mg_3P_2O_8$, which are 987 and 1029 cm^{-1} respectively.[69] This is a consequence of the fact that the PO_4 tetrahedron is nearly identical in orthophosphates. The Raman and IR spectra of the HP phase are qualitatively similar to those of the LP phase. The main difference is the decrease of the phonon gap which in the HP phase is between 625 and 880 cm^{-1}. We also notice a decrease of the frequency of the internal stretching modes, which in the HP phase are 940.4 and 1027.2 cm^{-1}. Similar decrease in frequency of these modes is found when comparing the Raman spectra of farringtonite-type and chopinite-type $Mg_3P_2O_8$.[69] Such decrease in the frequency of phonon modes is related to the distortion of the PO_4 tetrahedron.

IV. Conclusions

Through high-pressure X-ray diffraction experiments and density-functional theory calculations it has been concluded that $Co_3P_2O_8$ experiences a phase transition beyond 2.9 GPa. The crystal structure of the new high-pressure phase has been determined. The occurrence of phase transition is connected to the presence of CoO_5 trigonal bipyramids in the low-pressure phase and the formation of an additional Co–O bond induced by compression. We have also established the pressure dependence of the unit-cell parameters and a room-temperature equation of state for each phase. The obtained bulk moduli are discussed in comparison with related orthophosphates. Calculations also give the details about the elastic constants and moduli, and phonon frequencies, they may be important roles for using $Co_3P_2O_8$ in various applications.

Author contributions

Robin Turnbull, Josu Sánchez Martín, Akun Liang, Daniel Díaz-Anichtchenko, Catalin Popescu, K. Sandeep Rao, S. Nagabhusan Achary, and Alfonso Muñoz: investigation, writing – review & editing. Vinod Panchal: formal analysis, writing – review & editing. Daniel Errandonea: conceptualization, formal analysis, funding acquisition, investigation, project administration, writing – original draft, writing – review & editing.

Data availability

All relevant data are available from the corresponding author upon reasonable request.

Conflicts of interest

The authors declare that they have no known competing financial interests or personal relationships that could have appeared to influence the work reported in this paper.

Acknowledgements

References

1 D. Errandonea and A. B. Garg, Recent progress on the characterization of the high-pressure behaviour of AVO$_4$ orthovanadates, *Prog. Mater. Sci.*, 2018, **97**, 123–169, DOI: **10.1016/j.pmatsci.2018.04.004**.

2 K. Sugiyam and M. Tokonami, The crystal structure refinement of the strontium and barium orthophosphates, *Mineral. Mag.*, 1990, **15**, 141–146.

3 A. Grzechnik and P. F. McMillan, High Pressure Behavior of Sr$_3$(VO$_4$)$_2$ and Ba$_3$(VO$_4$)$_2$, *J. Solid State Chem.*, 1997, **132**, 156–162, DOI: **10.1006/jssc.1997.7435**.

4 O. R. Ankinapalli, B. N. Vamsi Krishna, R. R. Ayyaluri and J. S. Yu, Hydrothermal synthesis of high-performance cobalt phosphate nanorod architecture as bifunctional electrocatalysts for rechargeable Zn-air batteries and supercapatteries, *Mater. Today Sustain.*, 2024, **27**, 100863, DOI: **10.1016/j.mtsust.2024.100863**.

5 Z. Ristic, W. Piotrowski, M. Medic, J. Perisa, Z. M. Antic, L. Marciniak and M. D. Dramicanin, Near-Infrared Luminescent Lifetime-Based Thermometry with Mn^{5+}-Activated Sr$_3$(PO$_4$)$_2$ and Ba$_3$(PO$_4$)$_2$ Phosphors, *ACS Appl. Electron. Mater.*, 2022, **4**, 1057–1062, DOI: **10.1021/acsaelm.1c01207**.

6 W. M. Piotrowski, R. Marin, M. Szymczak, E. Martın Rodrıguez, D. H. Ortgies, P. Rodrıguez-Sevilla, P. Bolek, M. D. Dramicanin, D. Jaque and L. Marciniak, Critical evaluation of the thermometric performance of ratiometric luminescence thermometers based on Ba$_3$(VO$_4$)$_2$:Mn^{5+}, Nd^{3+} for deep-tissue thermal imaging, *J. Mater. Chem. C*, 2023, **11**, 6713–6723, DOI: **10.1039/d3tc00249g**.

7 J. S. Helton, N. Rogado, R. J. Cava and J. W. Lynn, Entropy driven incommensurate structures in the frustrated kagome staircase Co$_3$V$_2$O$_8$, *J. Phys.: Condens. Matter*, 2024, **36**, 205801, DOI: **10.1088/1361-648X/ad266b**.

8 K. Fritsch, G. Ehlers, K. C. Rule, K. Habicht, M. Ramazanoglu, H. A. Dabkowska and B. D. Gaulin, Quantum phase transitions and decoupling of magnetic sublattices in the quasi-two-dimensional Ising magnet Co$_3$V$_2$O$_8$ in a transverse magnetic field, *Phys. Rev. B: Condens. Matter Mater. Phys.*, 2015, **92**, 180404.

9 M. J. Jing, Y. C. Yang, Y. R. Zhu, H. S. Hou, Z. B. Wu and X. B. Ji, *Electrochim. Acta*, 2014, **14**, 234–240.

10 P. Suesse and M. J. Buerger, The structure of Ba$_3$(VO$_4$)$_2$, *Z. Kristallogr.*, 1970, **131**, 161–174, DOI: **10.1524/zkri.1970.131.16.161**.

11 S. Kesari, R. Rao and G. Balakrishnan, Polarized Raman spectroscopic study and investigation of phonon modes of Co$_3$(VO$_4$)$_2$ at variable thermodynamic conditions, *Solid State Sci.*, 2024, **149**, 107449, DOI: **10.1016/j.solidstatesciences.2024.107449**.

12 J. Sánchez-Martín, J. Pellicer-Porres, A. Liang, J. Ibáñez, R. Oliva, C. Popescu, Z. He, P. Rodríguez-Hernández, A. Muñoz and D. Errandonea, High-Pressure Vibrational and Structural Properties of Ni$_3$V$_2$O$_8$ and Co$_3$V$_2$O$_8$ up to 20 GPa, *J. Phys. Chem. C*, 2023, **127**, 21684–21694, DOI: **10.1021/acs.jpcc.3c04019**.

13 D. Díaz-Anichtchenko, R. Turnbull, E. Bandiello, S. Anzellini, S. N. Achary and D. Errandonea, Pressure-induced chemical decomposition of copper orthovanadate (α-Cu$_3$V$_2$O$_8$), *J. Mater. Chem. C*, 2021, **9**, 13402–13409, DOI: **10.1039/D1TC02901K**.

14 D. Díaz-Anichtchenko, D. Santamaria-Perez, T. Marqueño, J. Pellicer-Porres, J. Ruiz-Fuertes, R. Ribes, J. Ibañez, S. N. Achary, C. Popescu and D. Errandonea, Comparative study of the high-pressure behavior of ZnV$_2$O$_6$, Zn$_2$V$_2$O$_7$, and Zn$_3$V$_2$O$_8$, *J. Alloys Compd.*, 2020, **837**, 155505, DOI: **10.1016/j.jallcom.2020.155505**.

15 J. Sánchez-Martín, D. Errandonea, H. S. R. Mosafer, W. Paszkowicz, R. Minikayev, R. Turnbull, M. Berkowski, J. Ibáñez-Insa, C. Popescu, A. Fitch, P. Rodríguez-Hernández and A. Muñoz, The pressure and temperature evolution of the Ca$_3$V$_2$O$_8$ crystal structure using powder X-ray diffraction, *CrystEngComm*, 2023, **25**, 1240–1251, DOI: **10.1039/D2CE01676A**.

16 S. Kesari, A. B. Garg, O. Clemens, B. Joseph and R. Rao, Pressure-Induced Structural Behavior of Orthorhombic Mn3(VO4)2: Raman Spectroscopic and X-ray Diffraction Investigations, *ACS Omega*, 2022, **7**, 3099–3108, DOI: **10.1021/acsomega.1c06590**.

17 D. Diaz-Anichtchenko, E. Bandiello, J. Gonzáles-Platas, A. Liang, Z. He, A. Muñoz, P. Rodríguez-Hernández, D. Errandonea and C. Popescu, Physical Properties and Structural Stability of Cobalt Pyrovanadate Co$_2$V$_2$O$_7$ under High-Pressure Conditions, *J. Phys. Chem. C*, 2022, **126**, 13416–13426, DOI: **10.1021/acs.jpcc.2c03101**.

18 R. Turnbull, J. González-Platas, F. Rodríguez, A. Liang, C. Popescu, Z. He, D. Santamaría-Pérez, P. Rodríguez-Hernández, A. Muñoz and D. Errandonea, Pressure-Induced Phase Transition and Band Gap Decrease in Semiconducting β-Cu2V2O7, *Inorg. Chem.*, 2022, **61**, 3697–3707, DOI: **10.1021/acs.inorgchem.1c03878**.

19 P. B. Moore, Sarcopside: its atomic arrangement, *Am. Mineral.*, 1972, **57**, 24–35.

20 H. Annersten and A. G. Nord, A high pressure phase of magnesium orthophosphate, *Acta Chem. Scand., Ser. A*, 1980, **34**, 389–390.

21 R. W. Bild, New occurrences of phosphates in iron meteorites, *Contrib. Mineral. Petrol.*, 1974, **45**, 91–98.

22 C. Floss, Fe,Mg,Mn-bearing phosphates in the GRA 95209 meteorite: Occurrences and mineral chemistry, *Am. Mineral.*, 1999, **84**, 1354–1359, DOI: 10.2138/am-1999-0912.

23 E. S. Grew, T. Armbruster, O. Medenbach, M. G. Yates, C. Carson and J. Christopher, Chopinite, $(Mg,Fe)_3(PO_4)_2$, a new mineral isostructural with sarcopside, from a fluorapatite segregation in granulite-facies paragneiss, Larsemann Hills, Prydz Bay, East Antarctica, *Eur. J. Mineral.*, 2007, **2**, 229–245, DOI: 10.1127/0935-1221/2007/0019-1712.

24 A. G. Nord and T. Stefanidis, Structure refinements of $Co_3(PO_4)_2$. A note on the reliability of powder diffraction studies, *Acta Chem. Scand., Ser. A*, 1983, **37**, 715–721.

25 F. Hatert, E. Roda-Robles, P. d. Parseval and J. Wouters, ZAVALÍAITE, $(Mn^{2+},Fe^{2+},Mg)_3(PO_4)_2$, A new member of the sarcopside group from the La Empleada Pegmatite, San Luis province, Argentina, *Can. Mineral.*, 2012, **50**, 1445–1452, DOI: 10.3749/canmin.50.6.1445.

26 F. Brunet and D. Vielzeuf, The farringtonite/$Mg_3(PO_4)_2$-II transformation: A new curve for pressure calibration in piston cylinder apparatus, *Eur. J. Mineral.*, 1996, **8**, 349–354.

27 B. Berthet, J. C. Joubert and E. F. Bertaut, Vacancies ordering in new metastable orthophosphates [Co3]P2O8 and [Mg3]P2O8 with olivin-related structure, *Z. Kristallogr. - Cryst. Mater.*, 1972, **136**, 98–105, DOI: 10.1524/zkri.1972.136.16.98.

28 I. Loa, A. Grzechnik, U. Schwarz, K. Syassen, M. Hanfland and R. K. Kremer, Vanadium oxides V_2O_5 and NaV_2O_5 under high pressures: Structural, vibrational, and electronic properties, *J. Alloys Compd.*, 2001, **317–318**, 103–108, DOI: 10.1016/S0925-8388(00)01404-3.

29 F. Therrien, E. B. Jones and V. Stevanović, Metastable materials discovery in the age of large-scale computation featured, *Appl. Phys. Rev.*, 2021, **8**, 031310, DOI: 10.1063/5.0049453.

30 J. B. Anderson, E. Kostiner, M. C. Miller and J. R. Rea, The Crystal Structure of Cobalt Orthophosphate $Co_3(PO_4)_2$, *J. Solid State Chem.*, 1975, **14**, 372–377, DOI: 10.1016/0022-4596(75)90058-4.

31 C. Calvo, The crystal structure and luminescence of gamma-zinc orthophosphate, *J. Phys. Chem. Solids*, 1963, **24**, 141–149.

32 A. G. Nord and P. Kierkegaard, The crystal structure of $Mg_3(PO_4)_2$, *Acta Chem. Scand.*, 1968, **122**, 1466–1474.

33 M. A. Tena, R. Mendoza, C. Trobajo and S. García-Granda, Cobalt Minimisation in Violet $Co_3P_2O_8$ Pigment, *Materials*, 2022, **15**, 1111, DOI: 10.3390/ma15031111.

34 H. Keil, M. Hellström, C. Stückl, R. Herbst-Irmer, J. Behler and D. Stalke, New Insights into the Catalytic Activity of Cobalt Orthophosphate $Co_3(PO_4)_2$ from Charge Density Analysis, *Chem. – Eur. J.*, 2019, **25**, 15786, DOI: 10.1002/chem.201902303.

35 J.-J. Li, M.-C. Liu, L.-B. Kong, M. Shi, W. Han and L. Kang, Facile synthesis of $Co_3P_2O_8·8H_2O$ for high-performance electrochemical energy storage, *Mater. Lett.*, 2015, **161**, 404–407, DOI: 10.1016/j.matlet.2015.09.001.

36 J. B. Forsyth, C. Wilkinson, S. Paster and B. M. Wanklyn, Antiferromagnetism in cobalt orthophosphate, *J. Phys. C: Solid State Phys.*, 1988, **21**, 2005, DOI: 10.1088/0022-3719/21/10/018.

37 L. V. Shvanskaya, O. S. Volkova and A. N. Vasiliev, A review on crystal structure and properties of 3d transition metal (II) orthophosphates $M_3(PO_4)_2$, *J. Alloys Compd.*, 2020, **835**, 155028, DOI: 10.1016/j.jallcom.2020.155028.

38 F. Fauth, I. Peral, C. Popescu and M. Knapp, The new material science powder diffraction beamline at ALBA synchrotron, *Powder Diffr.*, 2013, **28**, S360–S370, DOI: 10.1017/S0885715613000900.

39 S. Klotz, J. C. Chervin, P. Munsch and G. Le Marchand, Hydrostatic limits of 11 pressure transmitting media, *J. Phys. D: Appl. Phys.*, 2009, **42**, 075413, DOI: 10.1088/0022-3727/42/7/075413.

40 D. Errandonea, A. Muñoz, P. Rodríguez-Hernández, O. Gomis, S. N. Achary, C. Popescu, S. J. Patwe and A. K. Tyagi, High-Pressure Crystal Structure, Lattice Vibrations, and Band Structure of $BiSbO_4$, *Inorg. Chem.*, 2016, **55**, 4958–4969, DOI: 10.1021/acs.inorgchem.6b00503.

41 A. Dewaele, P. Loubeyre and M. Mezouar, Equations of state of six metals above 94 GPa, *Phys. Rev. B: Condens. Matter Mater. Phys.*, 2004, **70**, 094112, DOI: 10.1103/PhysRevB.70.094112.

42 C. Prescher and V. B. Prakapenka, DIOPTAS: a program for reduction of two-dimensional X-ray diffraction data and data exploration, *High Pressure Res.*, 2015, **35**, 223–230, DOI: 10.1080/08957959.2015.1059835.

43 J. Rodríguez-Carvajal, Recent advances in magnetic structure determination by neutron powder diffraction, *Phys. B*, 1993, **192**, 55–69, DOI: 10.1016/0921-4526(93)90108-I.

44 P. Hohenberg and W. Kohn, Inhomogeneous Electron Gas, *Phys. Rev.*, 1964, **136**, B864–B871, DOI: 10.1103/PhysRev.136.B864.

45 G. Kresse and J. Furthmüller, Efficiency of *ab initio* total energy calculations for metals and semiconductors using a plane-wave basis set, *Comput. Mater. Sci.*, 1996, **6**, 15–50, DOI: 10.1016/0927-0256(96)00008-0.

46 G. Kresse and J. Furthmüller, Efficient iterative schemes for ab initio total-energy calculations using a plane-wave basis set, *Phys. Rev. B: Condens. Matter Mater. Phys.*, 1996, **54**, 11169–11186, DOI: 10.1103/PhysRevB.54.11169.

47 P. E. Blöchl, Projector augmented-wave method, *Phys. Rev. B: Condens. Matter Mater. Phys.*, 1994, **50**, 17953–11979, DOI: 10.1103/PhysRevB.50.17953.

48 G. Kresse and D. Joubert, From ultrasoft pseudopotentials to the projector augmented-wave method, *Phys. Rev. B: Condens. Matter Mater. Phys.*, 1999, **59**, 1758–1775, DOI: 10.1103/PhysRevB.59.1758.

49 R. Armiento and A. E. Mattsson, Functional designed to include surface effects in self-consistent density functional theory, *Phys. Rev. B: Condens. Matter Mater. Phys.*, 2005, **72**, 085108, DOI: 10.1103/PhysRevB.72.085108.

50 S. L. Dudarev, G. A. Botton, S. Y. Savrasov, C. J. Humphreys and A. P. Sutton, Electron-Energy-Loss Spectra and the Structural Stability of Nickel Oxide: An LSDA+U Study, *Phys. Rev. B: Condens. Matter Mater. Phys.*, 1998, **57**, 1505–1509, DOI: **10.1103/PhysRevB.57.1505**.

51 D. Diaz-Anichtchenko, E. Bandiello, J. G. Gonzalez-Platas, A. Liang, H. Zhangzhen, D. Errandonea, C. Popescu, A. Muñoz and P. Rodriguez-Hernandez, Physical Properties and Structural Stability of Cobalt Pyrovanadate $Co_2V_2O_7$ under High-Pressure Conditions, *J. Phys. Chem. C*, 2022, **126**, 13416–13426, DOI: **10.1021/acs.jpcc.2c03101**.

52 F. Birch, Finite Elastic Strain of Cubic Crystals, *Phys. Rev.*, 1947, **71**, 809–824, DOI: **10.1103/PhysRev.71.809**.

53 A. Togo and I. Tanaka, *Scr. Mater.*, 2015, **108**, 1–5, DOI: **10.1016/j.scriptamat.2015.07.021**.

54 Y. L. Page and P. Saxe, Symmetry-general least-squares extraction of elastic data for strained materials from ab initio calculations of stress, *Phys. Rev. B: Condens. Matter Mater. Phys.*, 2002, **65**, 104104, DOI: **10.1103/PhysRevB.65.104104**.

55 E. Bandiello, D. Errandonea, J. Pellicer-Porres, A. B. Garg, P. Rodriguez-Hernandez, A. Muñoz, D. Martinez-Garcia, R. Rao and C. Popescu, Effect of High Pressure on the Crystal Structure and Vibrational Properties of Olivine-Type $LiNiPO_4$, *Inorg. Chem.*, 2018, **57**, 10265–10276, DOI: **10.1021/acs.inorgchem.8b01495**.

56 A. Boultif and D. Louër, Powder pattern indexing with the dichotomy method, *J. Appl. Crystallogr.*, 2004, **37**, 724–731, DOI: **10.1107/s0021889804014876**.

57 N. V. Chandra Shekar and K. Govinda Rajan, Kinetics of pressure induced structural phase transitions: A review, *Bull. Mater. Sci.*, 2001, **24**, 1–21, DOI: **10.1007/BF02704834**.

58 T. Q. Tan, R. A. M. Osman, Z. A. Z. Jamal, M. V. Reddy and M. S. Idris, Structure and electrical properties of solid solution $Li[Ni_{0.5}Mn_{0.5}]_{1-x}Co_xPO_4$ ($1 \geq x \geq 0$), *Mater. Sci. Eng., B*, 2019, **241**, 55–65, DOI: **10.1016/j.mseb.2019.02.005**.

59 K. Lejaeghere, L. Vanduyfhuys, T. Verstraelen, V. Van Speybroeck and S. Cottenier, Is the error on first-principles volume predictions absolute or relative?, *Comput. Mater. Sci.*, 2016, **117**, 390–396, DOI: **10.1016/j.commatsci.2016.01.039**.

60 A. Wang, R. Kingsbury, M. McDermott, M. Horton, A. Jain, S. P. Ong, S. Dwaraknath and K. A. Persson, A framework for quantifying uncertainty in DFT energy corrections, *Sci. Rep.*, 2021, **11**, 15496, DOI: **10.1038/s41598-021-94550-5**.

61 P. R. Scott, J. A. Crow, R. Z. LeGeros and M. B. Kruger, A pressure-induced amorphous phase transition in magnesium-substituted-tricalcium phosphate, *Solid State Commun.*, 2011, **151**, 1609–1611, DOI: **10.1016/j.ssc.2011.07.019**.

62 C. Leyx, P. Schmid-Beurmann, F. Brunet, C. Chopin and C. Lathe, Compressibility and thermal expansion of magnesium phosphates, *Eur. J. Mineral.*, 2024, **36**, 417–431, DOI: **10.5194/ejm-36-417-2024**.

63 S. Zhai, W. Xue, D. Yamazaki, S. Shan, E. Ito, N. Tomioka, A. Shimojuku and K. Funakoshi, Compressibility of strontium orthophosphate $Sr3(PO4)2$ at high pressure, *Phys. Chem. Miner.*, 2011, **38**, 357–361, DOI: **10.1007/s00269-010-0409-9**.

64 D. Errandonea, S. N. Achary, D. Diaz-Anichtchenko, E. Bandiello, T. Marqueño, R. Shukla, A. K. Tyagi, C. Popescu and F. G. Alabarse, Equations of State and Crystal Structures of $KCaPO4$, $KSrPO4$, and $K_2Ce(PO_4)_2$ under High Pressure: Discovery of a New Polymorph of $KCaPO4$, *Cryst. Growth Des.*, 2023, **23**, 2782–2794, DOI: **10.1021/acs.cgd.2c0154**.

65 G. Grimvall, B. Magyari-Köpe, V. Ozoliņš and K. A. Persson, Lattice instabilities in metallic elements, *Rev. Mod. Phys.*, 2012, **84**, 945–986, DOI: **10.1103/RevModPhys.84.945**.

66 D. H. Chung and W. R. Buessem, The Voigt–Reuss–Hill Approximation and Elastic Moduli of Polycrystalline MgO, CaF_2, β–ZnS, ZnSe, and CdTe, *J. Appl. Phys.*, 1967, **38**, 2535–2540, DOI: **10.1063/1.1709944**.

67 D. Errandonea, A. Muñoz and J. Gonzalez-Platas, Comment on "High-pressure X-ray diffraction study of YBO_3/Eu^{3+}, $GdBO_3$, and $EuBO_3$: Pressure-induced amorphization in $GdBO_3$" [J. Appl. Phys. 115, 043507 (2014)], *J. Appl. Phys.*, 2014, **115**, 216101, DOI: **10.1063/1.4881057**.

68 S. F. Pugh, Relations between the elastic moduli and the plastic properties of polycrystalline pure metals, *Philos. Mag.*, 1954, **45**, 823–843, DOI: **10.1080/14786440808520496**.

69 X. Hu, L. Liu and S. Zhai, The structure-Raman spectra relationships of $Mg_3(PO_4)_2$ polymorphs: A comprehensive experimental and DFT study, *Spectrochim. Acta, Part A*, 2021, **245**, 118906, DOI: **10.1016/j.saa.2020.118906**.

70 S. Zhai, X. Wu and E. Ito, High-pressure Raman spectra of tuite, γ -$Ca_3(PO_4)_2$, *J. Raman Spectrosc.*, 2010, **41**, 1011–1013, DOI: **10.1002/jrs.2522**.